Journal of Materials Chemistry B

ROYAL SOCIETY OF CHEMISTRY

PAPER

View Article Online
View Journal | View Issue

Cite this: J. Mater. Chem. B, 2023, 11, 8528

NIR-II fluorescence and PA imaging guided activation of STING pathway in photothermal therapy for boosting cancer immunotherapy by theranostic thermosensitive liposomes†

Qi Long,‡[a] Yuliang Yang,‡[b] Fangling Liao,[a] Haoting Chen,[a] Dongyue He,[a] Shengliang Li,[b] Pengcheng Li,*[c] Weisheng Guo *[a] and Yafang Xiao*[a]

Received 1st April 2023,
Accepted 3rd August 2023

DOI: 10.1039/d3tb00711a

rsc.li/materials-b

Photothermal immunotherapy has shown great potential for efficient cancer treatment. However, the immunosuppressive tumor microenvironment forms a heavy barrier for photothermal-induced anti-tumor immunity by inhibiting dendritic cell (DC) maturation and cytotoxic T cell response. Moreover, the lack of reliable spatiotemporal imaging modalities makes photothermal immunotherapy difficult to guide tumor ablation and monitor therapeutic outcomes in real time. Herein, we designed a theranostic thermosensitive liposome (PLDD) as a versatile nanoplatform to boost the adaptive anti-tumor immunity of photothermal immunotherapy and to achieve multiple bioimaging modalities in a real-time manner. PLDD contains two major functional components: a multifunctional photothermal agent (DTTB) and an immune potentiator STING pathway agonist (DMXAA). Upon irradiation, the heat generated by DTTB induced the immunogenic cell death (ICD) of the tumor and dissociated the structure of thermosensitive liposome to release DMXAA, which ultimately activated the STING pathway and promoted the ICD-induced immune response by increasing DC cell maturation and T cell recruitment. Moreover, the DTTB in PLDD displayed excellent second near-infrared (NIR-II) fluorescence and photoacoustic (PA) dual-modal imaging, which provided omnibearing information on the tumor and guided the subsequent therapeutic operation. Therefore, this versatile PLDD with light-triggered promotion of anti-tumor immunity and multiple spatiotemporal imaging profiles holds great potential for the future development of cancer immunotherapy.

1. Introduction

Photothermal therapy (PTT) has been considered one of the most promising strategies for localized tumor ablation by transferring the photoenergy into heat.[1–3] However, the dilemma for current PTT is that excessive temperature can completely ablate the tumor but cause irreversible damage to surrounding healthy tissues, while mild temperature shows fewer adverse effects but a considerable risk of tumor recurrence.[4] To address these challenges, PTT with mild heat has been recently integrated with immunotherapy to potentiate anti-tumor immune response.[5–7] Upon irradiation, hyperthermia generated by PTT arouses the immunogenic cell death (ICD) of tumor cells and releases tumor-associated antigens (TAAs) and damage-associated molecular patterns (DAMPs), which activate the anti-tumor immune response and effectively reverse the immunosuppressive tumor microenvironment by elevating the antigen-specific T cell response and activation and enhancing the antigen-presenting ability and maturation of dendritic cells (DCs).[8–11] Although PTT can induce the ICD of tumor cells, the immunosuppressive tumor microenvironment is still a significant barrier to the enhancement of anti-tumor immune response by inhibiting DC maturation and cytotoxic T cell response, which considerably compromises the therapeutic effect of the combined immunotherapy.[12,13]

The stimulator of interferon genes (STING) DNA sensing pathway has been proven as an effective immunotherapy target for potent local immune stimulation to many highly

[a] Department of Minimally Invasive Interventional Radiology, School of Biomedical Engineering & The Second Affiliated Hospital, Guangzhou Medical University, Guangzhou, 510260, P. R. China. E-mail: tjuguoweisheng@126.com, yafangxiao@gzhmu.edu.cn
[b] College of Pharmaceutical Sciences, Soochow University, Suzhou 215123, P. R. China
[c] Department of Orthopedics Trauma and Microsurgery, Zhongnan Hospital of Wuhan University, Wuhan, Hubei, 430071, P. R. China. E-mail: lpc0730@whu.edu.cn

† Electronic supplementary information (ESI) available. See DOI: https://doi.org/10.1039/d3tb00711a

‡ Equally contributed.

immunosuppressive tumors, such as brain tumor glioblastoma.[14–18] The activated STING pathway produces type I interferon (IFN), recruits TANK binding kinase 1 (TBK1), and up-regulates the expression of interferon regulatory factor 3 (IRF3), signal transducer and activator of transcription 6 (STAT6), an inhibitor of kappa-B kinase (IKK) and various pro-inflammatory cytokines.[19–21] Thus, STING agonist can promote DC maturation, accelerate antigen presentation, activate T cells, and induce tumor cell apoptosis, and eventually initiating the anti-tumor immunity for cancer treatment.[22,23] However, the therapeutic effect of STING agonist is compromised owing to the rapid plasma clearance, poor membrane permeability, and low accumulation in the tumor.[24–27] Drug delivery systems (DDSs) based on nanotechnology present a great potential to intelligently control the release of drugs, which can protect the drug from premature degradation, optimize the pharmacokinetic profile and manipulate drug distribution in tissues. DDSs with smart drug carriers can release active ingredients at appropriate sites in response to certain physiological variables or external physicochemical stimuli, such as pH, enzyme, light, heat, magnetic force, and ultrasound.[28–30] Therefore, developing an intelligent drug delivery system of STING agonist with controlled release is an urgent need to boost the anti-tumor immunity of photothermal immunotherapy.

With the development of photothermal immunotherapy in clinical applications, it is vital to develop reliable imaging modalities for photothermal immunotherapy to accomplish a theranostic platform.[31,32] Compared with fluorescence imaging in the visible and first near-infrared (NIR-I) region, the second near-infrared (NIR-II, 1000–1700 nm) fluorescence displays deeper penetration depth, reduced photon scattering, lower tissue background, and higher temporal-spatial resolution, which is more suitable for deep-seated tumors imaging.[33–35]

Weisheng Guo

Weisheng Guo is a professor in the School of Biomedical Engineering at Guangzhou Medical University since 2018. He received his PhD in Materials Science from Tianjin University in 2015. He received research training at the National Institutes of Health (NIH) in the US as a joint PhD student for 2 years. His research goal is to develop cellular bioengineering nanomaterials by leveraging the power of synthetic material chemistry and synthetic biology to achieve potent immune therapy and immunity evaluation for cancers, autoimmune diseases, and atherosclerosis. Dr Guo as the first/corresponding author has published more than 50 papers in the field's top journals, such as Nature Nanotechnology, Science Advances, Nature Communications, Advanced Materials, ACS Nano, Advanced Functional Materials, and Nano Letters.

Photoacoustic (PA) imaging is another bioimaging technique for the focal plane of tissue, which can achieve deep (5–7 cm) tissue imaging with high spatial resolution.[36] However, most photothermal agents usually have PA imaging but weak or no NIR-II fluorescence.[37,38] Therefore, developing a photothermal nanomedicine with NIR-II fluorescence and PA imaging can provide omnibearing tumor information and guide the subsequent therapeutic operation in anti-tumor photothermal immunotherapy.

In this study, we designed versatile theranostic thermosensitive liposomes (TSL), denoted as PLDD, for boosting cancer photothermal immunotherapy guided by NIR-II fluorescence and PA dual-modal imaging (Scheme 1). The skeleton of TSL was constructed using liposome (DSPE-PEG-2K and lecithin) and phase change materials (lauric acid and stearic acid).[39] A NIR-II donor–acceptor–donor oligomer (DTTB), which was previously reported by our group, was integrated into the TSL as a photothermal and bioimaging agent.[40] Owing to the effective NIR-II fluorescent core (benzobisthiadiazole) and strong donor–acceptor conjugation, DTTB can efficiently produce heat and display excellent NIR-II fluorescence and PA dual-modal imaging upon irradiation. The STING agonist, DMXAA, was loaded inside the TSL as an immune potentiator. Upon laser irradiation, the heat generated by DTTB induced the ICD of tumor cells and disrupted the TSL structure to release DMXAA. The release of DMXAA activated the STING pathway and significantly promoted the ICD-induced immune response by increasing DC cell maturation and T cell recruitment in tumors. Ultimately, the *in vivo* experiment results showed that PLDD achieved an excellent anti-tumor effect on murine lung cancer through boosted photothermal immunotherapy, with the guidance of effective NIR-II fluorescence and PA dual-modal imaging. Thus, this versatile theranostic TSL with a light-triggered elevation of anti-tumor immunity and spatiotemporal imaging profiles will provide a new perspective for cancer photothermal immunotherapy.

2. Experimental section

2.1 Materials and reagents

All reagents and solvents were of analytical grade and used as received. Soybean lecithin was purchased from Shanghai Yuanye Bio-Technology Co., Ltd. Stearic acid was obtained from Sigma-Aldrich. Lauric acid (97%) and DMXAA (Vadimezan) were purchased from Shanghai Aladdin Bio-Chem Technology Co., LTD. PEG2000-DSPE was purchased from MedChemExpress. Ethyl alcohol, methanol, tetrahydrofuran (THF), and dimethyl sulfoxide (DMSO) were provided by Shanghai Macklin Biochemical Technology Co., Ltd.

2.2 Preparation of PCM and PLDD

PCM was prepared by applying a nanoprecipitation method. First, lauric and stearic acids were dissolved in methanol at a ratio of 4 : 1. Lecithin and DSPE-PEG2000 were dissolved in a 4% aqueous ethanol solution at 1 mg mL^{-1} concentration and a 3 : 1 ratio. Then, we heated the phospholipid solution to

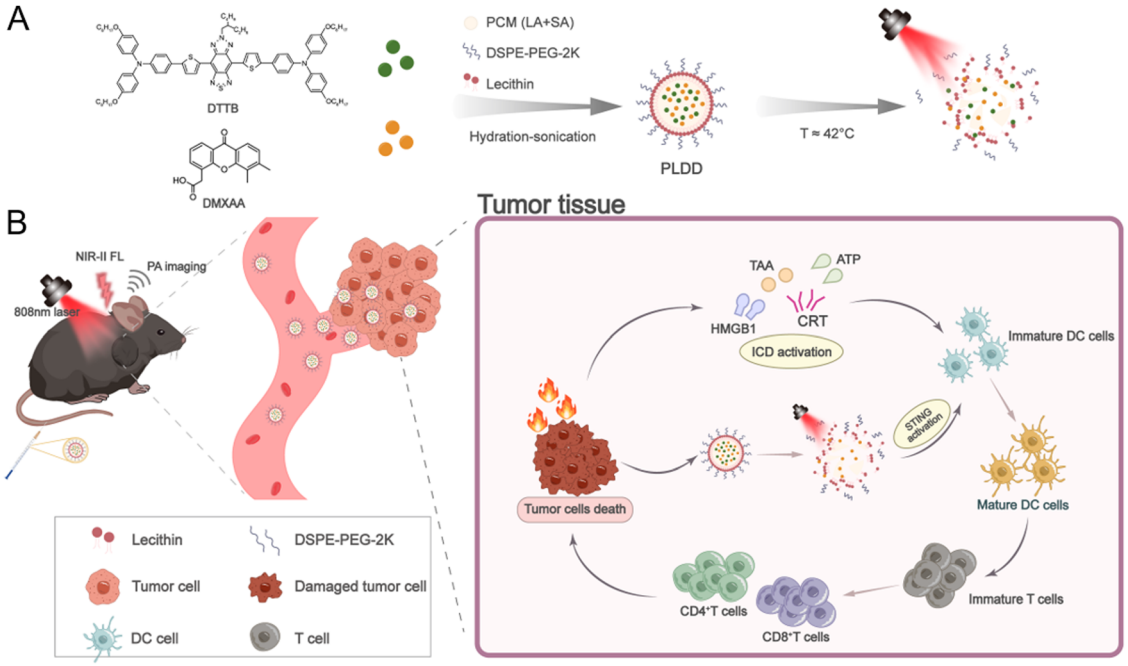

Scheme 1 Schematic illustration of multiple bioimaging-guided activations of the STING pathway in photothermal therapy for boosting cancer immunotherapy by theranostic PLDD. (A) Preparation of PLDD. (B) Activated STING pathway to promote ICD-mediated photothermal immunotherapy guided by NIR-II fluorescence and PA imaging dual modal imaging.

around 50 °C. The desired payloads (48 μL of 2.5 mg mL^{-1} DTTB in THF and 48 μL of 2.5 mg mL^{-1} DMXAA in DMSO) were added to 600 μL PCM solution and mixed well with ultrasonic. After that, we added the above solution dropwise into the preheated phospholipid solution with ultrasonic for 5 min. The nanoparticles were solidified in an ice bath for 2 minutes. After returning to room temperature, the large particles were removed by filtration membrane (0.22 μm), and the free excess components were removed by ultrafiltration tube (Sartorius, MWCO = 100 kDa) three times.

2.3 Evaluation of DMXAA release

200 μL of PLDD solution (20 μg mL^{-1} in PBS) was irradiated under an 808 nm (1 W cm^{-2}) laser for 5 min. After laser irradiation, 800 μL of PBS was added to the solution, and the mixed solution was filtered using an ultrafiltration tube (100 kDa). The lower layer of the solution was used for HPLC analysis with acetonitrile/water as the eluent at a detection wavelength of 286 nm to determine the DMXAA concentration. The free DMXAA and PLDD without light treatment were also analyzed by applying HPLC as control groups under the same conditions.

2.4 Photothermal effect of PLDD

The PLDD solution was dispersed into six concentrations (80, 40, 20, 10, 5 and 0 μg mL^{-1}) and irradiated with a wavelength of 808 nm laser for 5 minutes. Temperatures were monitored using an infrared imaging device (Fluke, Ti400) every 30 s. Subsequently, 200 μL PLDD (40 μg mL^{-1}) was taken into the centrifugal tube. Next, the PLDD were irradiated for 5 minutes with an 808 nm laser at 1, 0.75, 0.5 and 0.25 W cm^{-2} power densities. Temperatures were monitored using an infrared imaging device (Fluke, Ti400) every 30 s.

2.5 Cell viability assay

The cytotoxicity of PLDD was investigated using a cell counting kit-8 (CCK-8) assay (Beyotime). Microtiter plates with 96 wells were plated with LLC at a density of 5×10^4 per well, and the cells were seeded for adherent growth and treated 24 h later. Each well was added to 100 μL of PLDD drug of different concentrations and incubated for 4 h. The light group was exposed to an 808 nm laser for 5 min (1 W cm^{-2}) and incubated for 24 h. The OD value of the microplate reader was measured at 450 nm. The cells were treated with PBS as the control group.

2.6 Live/dead cell staining

LLC (2×105 per well) was incubated in confocal dishes for 24 h. Then, we divided them into five groups: PBS, PLDD, Laser, PLDT + L, and PLDD + L. We added PLDT/PLDD to the corresponding groups for 4 h of incubation. The irradiation condition is an 808 nm laser for 5 min (1 W cm^{-2}). The cells were washed with PBS three times and then treated with calcein AM (5 μL) and PI (10 μL). After incubation for 15 min, all samples were imaged by the CLSM.

2.7 Animal model

The LLC tumor xenograft models were established by subcutaneously injecting onto the flank of the female BALB/c nude mice (4–6 weeks) with 100 μL of 1×10^7 LLC cell suspension per mouse. All animal experiments were performed in compliance

with the Guide for the Care and Use of Laboratory Animals (China, GB/T 35892-2018). The animal protocol was approved by the Institutional Animal Care and Use Committees at the Guangzhou Medical University.

2.8 *In vivo* photoacoustic imaging and NIR-II fluorescence imaging

When the tumor volume was around 100 mm^3, the C57BL/6J mice bearing subcutaneous LLC tumors were injected with free DTTB (1 mg mL^{-1}, 100 μL) and PLDD (1 mg mL^{-1}, 100 μL) *via* intravenous injection. Then, we anesthetized the mice by inadvertent intrathecal injection of Zoletil 50 and serazine hydrochloride and put them on a heating pad to maintain their body temperature. The photoacoustic images were captured at selected time intervals (0, 6, 12, 24, and 24 h) under different laser excitations of 680, 710, 730, and 910 nm using the Vevo LAZR system (FUJIFILM VisualSonics, Toronto, Canada). The fluorescence imaging was performed at 0, 2, 12, 24 and 36 h after injection with a near-infrared two-region imager. The imaging conditions of small animal photoacoustic imaging equipment were set as follows: 808 nm excitation, 60 mW cm^{-2} power density, 1200 nm long-pass filter, and 300 ms exposure time.

2.9 Immunofluorescence staining

The changes in CRT, HMGB1 and γ-H2AX levels of tumor tissue were evaluated by immunofluorescence staining. LLC subcutaneous tumor bearing mice were constructed. When the tumor size was about 100 mm^3, the mice were divided into different groups, including PBS, PLDD, Laser, PLDT + L and PLDD + L. The dosage of PLDD/PLDT for mice was 500 μg mL^{-1}, 100 μL. After 12 h of administration, the mice in the Laser, PLDT + L and PLDD + L groups were irradiated by an 808 nm laser (1 W cm^{-2}) for 5 min. One day after the irradiation, the tumors were taken for immunofluorescence staining using anti-CRT, anti-HMGB1 and anti-γH2AX antibodies.

2.10 Western blot experiment

LLC cells were grown in six-well plates overnight, and PBS, PLDT and PLDT were added to every cell well. After 4 h of incubation, the light group was illuminated with an 808 nm laser (1 W cm^{-2}) for 5 min, and the cells were then incubated for 24 h. The cells were lysed using RAPA lysate for 30 min and then centrifuged to remove the protein supernatant. Samples were quantified for total protein using the BCA Protein Quantification kit, and 25 μL of loading buffer was added to 100 μL of the sample. After thorough mixing, the samples were boiled in boiling water at 100 °C for 10 min. After natural cooling, the samples were centrifuged and dumped into the bottom of the centrifuge tube. Western blot was used to analyze the expression of each protein in the total protein. The antibodies used in this experiment were anti-CRT, anti-HMGB1, anti-STING, anti-IRF3, anti-ρIRF3, and anti-GAPDH (Abcam Inc., Cambridge, MA, USA).

2.11 Detection of T cells and DC cells

LLC subcutaneous tumor bearing mice were constructed. When the tumor size was about 100 mm^3, the mice were divided into different groups: PBS, PLDD, Laser, PLDT + L and PLDD + L groups. The dosage for the mice was 500 μg mL^{-1}, 100 μL. After 12 h of administration, the mice in the Laser, PLDT + L and PLDD + L groups were illuminated under an 808 nm laser (1 W cm^{-2}) for 5 min. One day after the light exposure, single-cell suspensions were taken from the tumor and spleen. T cells in the spleen were stained with antibodies CD3, CD4 and CD8 for flow cytometry. DC cells in the tumor were stained with antibodies CD11c, CD86 and CD80 for flow cytometry.

2.12 *In vivo* antitumor treatments

When the tumor grew to about 70 mm^3, the mice were divided into five groups: PBS, PLDD, Laser, PLDT + L, and PLDD + L. The dose concentration for each mouse was 500 μg mL^{-1}, 100 μL. Mice in the light group were exposed to an 808 nm laser light (1 W cm^{-2}) for 5 min at 12 h after drug administration. Temperature changes were recorded with a thermal imager. Body weight and tumor volume were recorded daily during the 14 day treatments. Mice were sacrificed on the last day of the treatments, and the tumors were weighed and photographed. The heart, liver, spleen, lung and kidney of mice in each group were taken for H&E staining, and the blood was processed for blood routine and liver and kidney index detection.

2.13 Statistical analysis

Error bars were based on standard deviation (SD) and $n = 3$ or 6. The data are presented as Mean ± SD. Statistical analysis was performed following a two-tailed unpaired t test: $^{*}p < 0.05$, $^{**}p < 0.01$, $^{***}p < 0.001$, $^{****}p < 0.0001$.

3. Results and discussion

3.1 Preparation and characterization of PLDD

To fabricate TSL with a suitable phase transition temperature for controllable drug release, two-phase change components of TSL, named lauric acid (LA) and stearic acid (SA), were mixed in different ratios to adjust their phase transition temperatures. As shown in Fig. 1(A), a mixture of LA and SA with a mass ratio of 3 : 1 displayed a phase transition temperature of around 42 °C, which is suitable for mild heat-triggered drug release while avoiding hyperthermia injury. Based on this, we constructed our PLDD with phase change materials (LA : SA = 3 : 1), the NIR-II photothermal agent (DTTB), the STING agonist (DMXAA) and other materials for building liposome structure (DSPE-PEG2000 and lecithin) using hydration ultrasound (Scheme 1(A)). The size distribution of the PLDD nanosphere in 1 × PBS was 124 ± 2.81 nm measured by dynamic light scattering (DLS), which is consistent with the PLDD image of transmission electron microscopy (TEM). The relatively low polymer dispersity index (PDI) and TEM image indicate good dispersion and uniformity of PLDD in water (Fig. 1(B)). In addition, the size variation in PLDD in water was measured within a week, and no significant change in size was observed, demonstrating the good stability of PLDD in water (Fig. S1, ESI†).

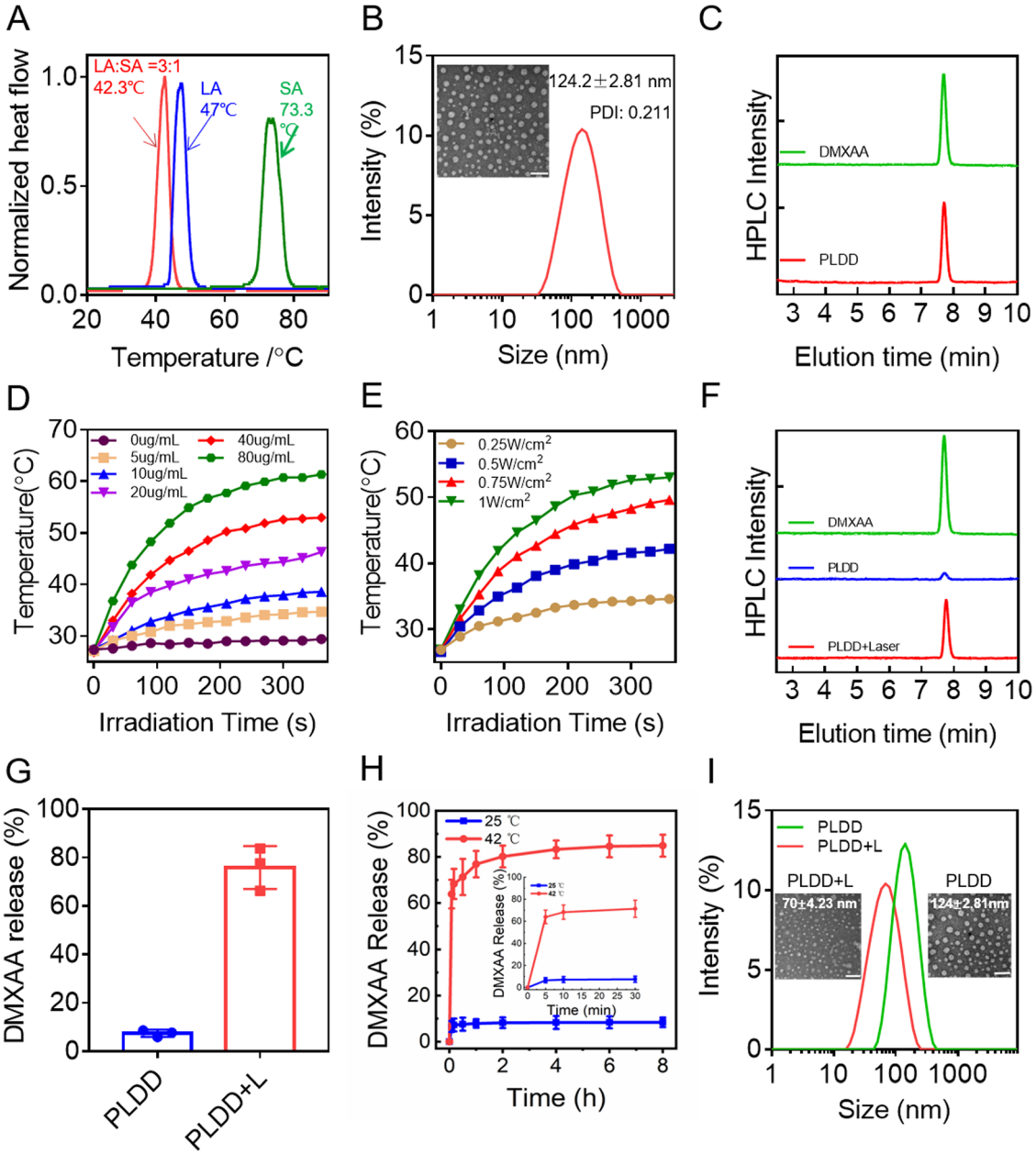

Fig. 1 Preparation and characterization of PLDD. (A) DSC curves of lauric acid, stearic acid, and a mixture of lauric and stearic acids at a 3 : 1 mass ratio. (B) TEM and DLS images of PLDD. Scale bars = 200 nm. (C) HPLC absorption curves of DMXAA and PLDD. (D) Temperature profiles of different concentrations of PLDD under irradiation. (E) Temperature profiles of 40 μg mL^{-1} PLDD under irradiation with different power densities. (F) HPLC absorption curves of DMXAA released from PLDD with or without irradiation. All samples were dispersed in 1 × PBS buffer for measurements. (G) Statistical plot of DMXAA release. n = 3. (H) Release curves of DMXAA from PLDD at different temperatures. (I) DLS and TEM of PLDD with or without irradiation.

The fluorescence spectrum of PLDD is mainly distributed in the NIR-II regions with a maximum emission at 915 nm and a tail towards 1300 nm (Fig. S2, ESI†). As shown in Fig. S3 (ESI†), the normalized absorbance of PLDD involves the typical absorbance peaks of DTTB and DMXAA, indicating the successful encapsulation of DTTB in PLDD. We further calculated the encapsulation efficiency and drug loading of DTTB and DMXAA by conducting high-performance liquid chromatography (HPLC) (Fig. 1(C)). The encapsulation efficiency and drug loading of DTTB were calculated as 93.67% and 5.6%, respectively, and those of DMXAA were 43.2% and 2.5%, respectively.

To evaluate the NIR-II-triggered drug release of PLDD, we first investigated its photothermal effect. Compared to the control group of deionized water, 80 μg mL^{-1} of PLDD can reach the phase transition temperature (42 °C) within a few seconds under NIR-II light irradiation, and the temperature continues to increase to 60.3 °C in 5 min, indicating their excellent photothermal effect (Fig. 1(D) and Fig. S4A, ESI†).

Moreover, the photothermal effect of PLDD showed a concentration/power dependent temperature variation under 808 nm laser irradiation (Fig. 1(D), (E) and Fig. S4B, ESI†). Then, the laser-triggered release performance of DMXAA was investigated through component analysis and size changes. As shown in Fig. 1(F), the DMXAA characteristic peak of PLDD significantly increased after laser irradiation for 5 min compared to PLDD without laser, as measured by HPLC, demonstrating the considerable release of free DMXAA in PLDD. The DMXAA release of PLDD upon irradiation was determined as 75.3% of the initial amount, which is almost a ten-fold increase than PLDD without laser (7.67%) (Fig. 1(G)). We then measured the release profile of DMXAA for 8 h at phase transition temperature (42 °C) and room temperature (25 °C), respectively. As shown in Fig. 1(H), almost 80% of DMAXX was released from PLDD within 1 h and then slowly released to nearly 90% over the next 7 h at 42 °C; however, less than 10% of DMXAA can be released from PLDD in 8 h at 25 °C. These results indicate the excellent thermosensitivity of PLDD for on-demand DMXAA release. Moreover, we measured the size change in PLDD before and after illumination. The results demonstrate that the size of PLDD decreased from 124 ± 2.81 nm to 70 ± 4.23 nm after laser irradiation, which is consistent with the corresponding TEM images (Fig. 1(I)). Therefore, the as-prepared PLDD displayed excellent photothermal response for laser triggered release of STING agonists, holding great potential for further *in vitro* and *in vivo* studies.

3.2 *In vitro* anti-tumor effect of PLDD

To evaluate the *in vitro* anti-tumor effect of PLDD, LLC cell viability measurements, including CCK-8, flow cytometry analysis, and live/dead cell staining, were conducted using PLDD and PLDT (without DMXAA) under irradiation. First, the LLC cells incubated with PLDT or PLDD for 24 h display little cytotoxicity without light (Fig. 2(A)), indicating their good biocompatibility. However, upon irradiation, both PLDD and PLDT show typical concentration-dependent cytotoxicity owing to their excellent photothermal effect (Fig. 2(B)). It is noteworthy that PLDD shows slightly better photo-cytotoxicity than PLDT, demonstrating that the release of the SING agonist promotes cell apoptosis. Then, the cell apoptosis of PLDD and PLDT was measured using an annexin V-FITC/PI co-staining assay by flow cytometry analysis and quantification (Fig. 2(C) and Fig. S5, ESI†). The results indicated that PLDT and PLDD did not induce cell apoptosis in the absence of light. However, the PLDT group with laser (PLDT + L) induced 22.1% and 29% of LLC cells in the early and late stages of apoptosis upon irradiation, respectively, and PLDD + L induced 16% and 43.3% of LLC cells in the early and late stages of apoptosis, respectively. Both PLDT and PLDD exerted good apoptotic induction performance under irradiation, and the release of DMXAA accelerated cell apoptosis to the late stage. To visually evaluate the *in vitro* anti-tumor effect of PLDD, the live/dead cell staining of LLC cells was further employed using the Calcein AM/PI co-staining assay in which the live cells were stained with Calcein AM (green fluorescence) and the dead cells were stained with PI (red fluorescence). As shown in Fig. 2(D), although both groups of PLDT + L and PLDD + L showed noticeable red fluorescence in the field, PLDD + L achieve more red fluorescence region than PLDT + L, indicating their excellent anti-tumor effect under irradiation.

3.3 Dual modal imaging and biodistribution of PLDD *in vivo*

In vivo NIR-II fluorescence and PA dual-modal imaging of PLDD were investigated in LLC tumor-bearing mice. For the PA imaging, we first tested the PA signal of the PLDD solution with different concentrations in small tubes, and the results showed that the PLDD solution displayed excellent PA signals with a good linear correlation between concentrations and signal intensities (Fig. 3(A) and (B)). The PA spectra of PLDD were scanned with full wavelength mode, and the peak appeared at around 714 nm (Fig. 3(C)). Then, we measured the *in vivo* PA signal of PLDD in LLC tumor-bearing mice. Compared with the free DTTB control group, PLDD showed a more intense signal because of the improved accumulation in the tumor, and the peak value appeared at 12 h after intravenous injection administration (Fig. 3(D) and (E)). For the NIR-II fluorescence imaging, we first tested the NIR-II fluorescence signals of PLDD solution with a series concentration using a 1200 nm long-pass filter under irradiation, and the PLDD solution displayed excellent NIR-II fluorescence signals with a good linear correlation between concentrations and signal intensities (Fig. S6A and B, ESI†). Then, PLDD was intravenously injected into the LLC tumor-bearing mice for *in vivo* NIR-II fluorescence imaging. As shown in Fig. 3(F), the NIR-II fluorescence signal of PLDD started to show a clear margin of the tumor after 6 h of administration, and the signal gradually reached its peak after 12 h of administration, consistent with the peak timing of PA imaging. Compared with the free DTTB control group, PLDD exhibited a stronger signal intensity and a longer retention time in the tumor, indicating its excellent tumor accumulation behavior. The improved accumulation of PLDD could be attributed to the advantages of the liposome drug delivery system, including PEGylation, negative surface charge and stable and controllable particle size, which provides a prolonged circulation time and stealth function for escape from the reticulo-endothelial system (RES).[41,42]

Moreover, the biodistribution of PLDD was investigated by performing a quantitative analysis for NIR-II fluorescence signals of the main organs and tumor of mice after 12 h of administration. As shown in Fig. 3(G) and Fig. S6C (ESI†), except for the liver and spleen, tumor ($13.78 \pm 1.62\%$) is the third highest site of accumulated PLDD, followed by lung, kidney and heart. PLDD accumulation is almost six-fold higher than free DTTB ($2.25 \pm 0.87\%$), indicating that their excellent pharmacokinetics are beneficial for anti-tumor treatment. However, more than 80% of free DTTB accumulated in the liver, lung and spleen, which are the major organs of RES (Fig. 3(G)). This is most likely attributed to the strong hydrophobicity of DTTB, making free DTTB aggregate into irregular large particles in the blood stream and quickly targeted and cleared out by RES. Moreover, the lack of protection against hydrophilic PEGylation decreases the blood circulation

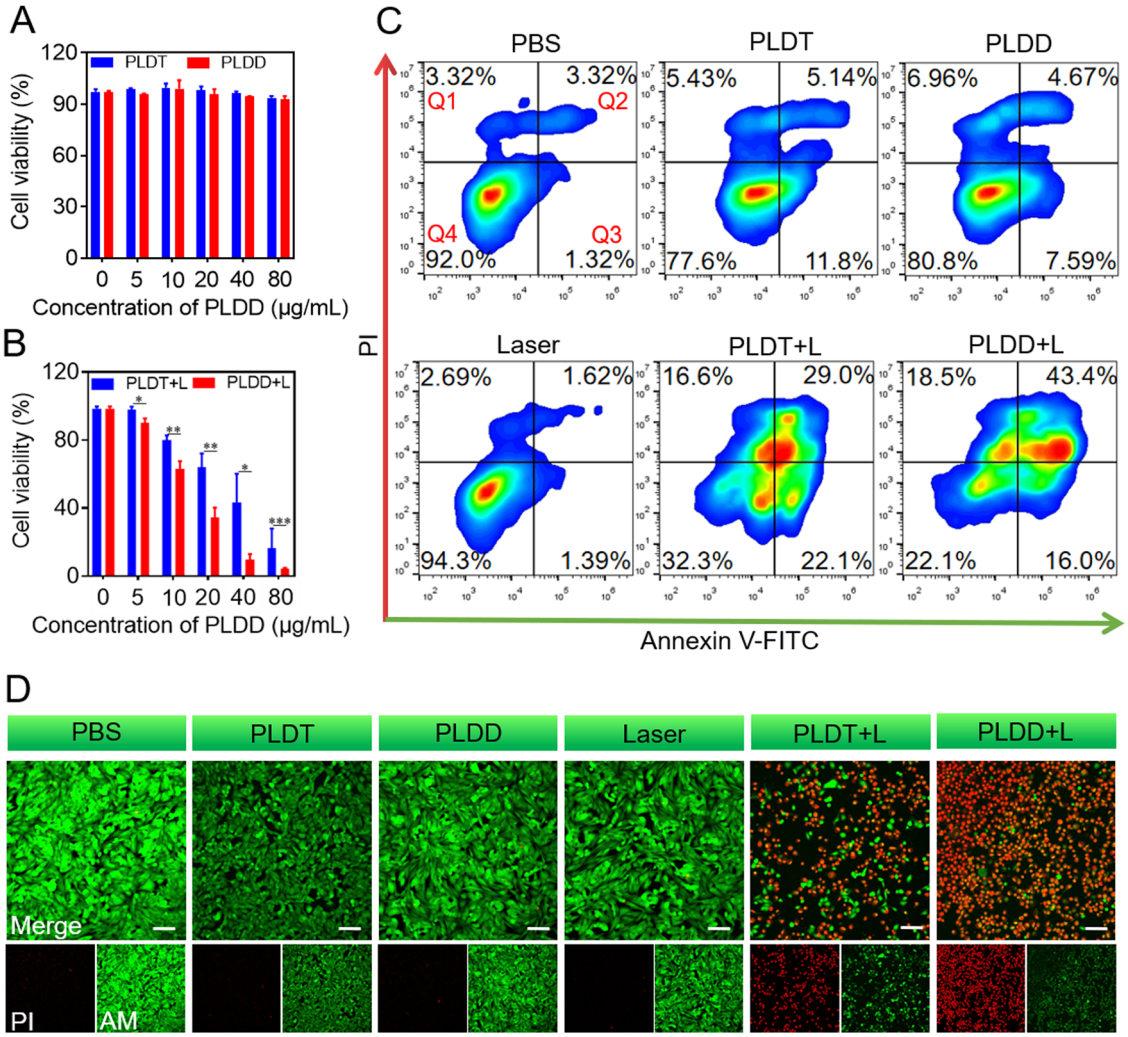

Fig. 2 *In vitro* antitumor effects of PLDD. (A) Dark cytotoxicity of LLC cells treated with PBS, PLDT, and PLDD. (B) Photo-cytotoxicity of LLC cells treated with PBS, PLDT, and PLDD under irradiation. (C) Flow cytometry analysis of LLC cell apoptosis treated with PBS, PLDT, and PLDD in the presence or absence of irradiation. Q1: necrocytosis; Q2: late stage of apoptosis; Q3: early stage of apoptosis; and Q4: living cell. (D) Fluorescent images of Calcein-AM/PI-stained LLC cells treated with PBS, PLDT, and PLDD and in the presence or absence of irradiation. The scale bar is 100 μm. L stands for laser. (*$p < 0.05$, **$p < 0.01$, ***$p < 0.001$).

time of free DTTB and increases the risk of being cleared out by RES.[43]

3.4 Boosted adaptive immune response of PLDD

To evaluate the boosted adaptive immune responses by PLDD during photothermal therapy, we first verified the PTT-induced ICD by measuring its typical biomarkers in PTT-treated LLC tumor-bearing mice, including calreticulin (CRT), high mobility group box 1 protein (HMGB1), and adenosine triphosphate (ATP).[44–46] Immunofluorescence assay was conducted to evaluate the levels of ICD-associated biomarkers in tumor sections with different treatments. The results suggested that the levels of CRT (green fluorescence) and HMGB1 (green fluorescence) significantly increased after treatment with PLDT + L and PLDD + L (Fig. 4(A)). We also measured the protein expression of CRT and HMGB1 in tumor cells after different treatments by western blot. As shown in Fig. 4(B), CRT expression increased while HMGB1 expression decreased in the PLDT + L and PLDD + L groups because the cell transferred CRT into the cell surface while releasing HMGB1 outside the cell during the PTT procedure. The ATP level was detected with the ATP ELISA kit, and cells treated with PLDT + L and PLDD + L displayed higher ATP levels than the other groups (Fig. 4(C)). The above results indicate that the photothermal effect of PLDD can successfully activate the ICD of tumor cells to further trigger adaptive antitumor immunity.

Then, we investigated the activation of the STING pathway by PLDD under irradiation cGAMP, a natural ligand for STING proteins, can be produced by recognizing cytoplasmic tumor DNA by cGAS. Binding cGAMP to STING induces translational changes in STING proteins, and activation of the downstream signaling cascade IRF-3, ultimately leading to the upregulation of type I interferon (*e.g.*, interferon-β) and activated $CD8^+$ T cells in the tumor microenvironment.[47] Therefore, the activation of

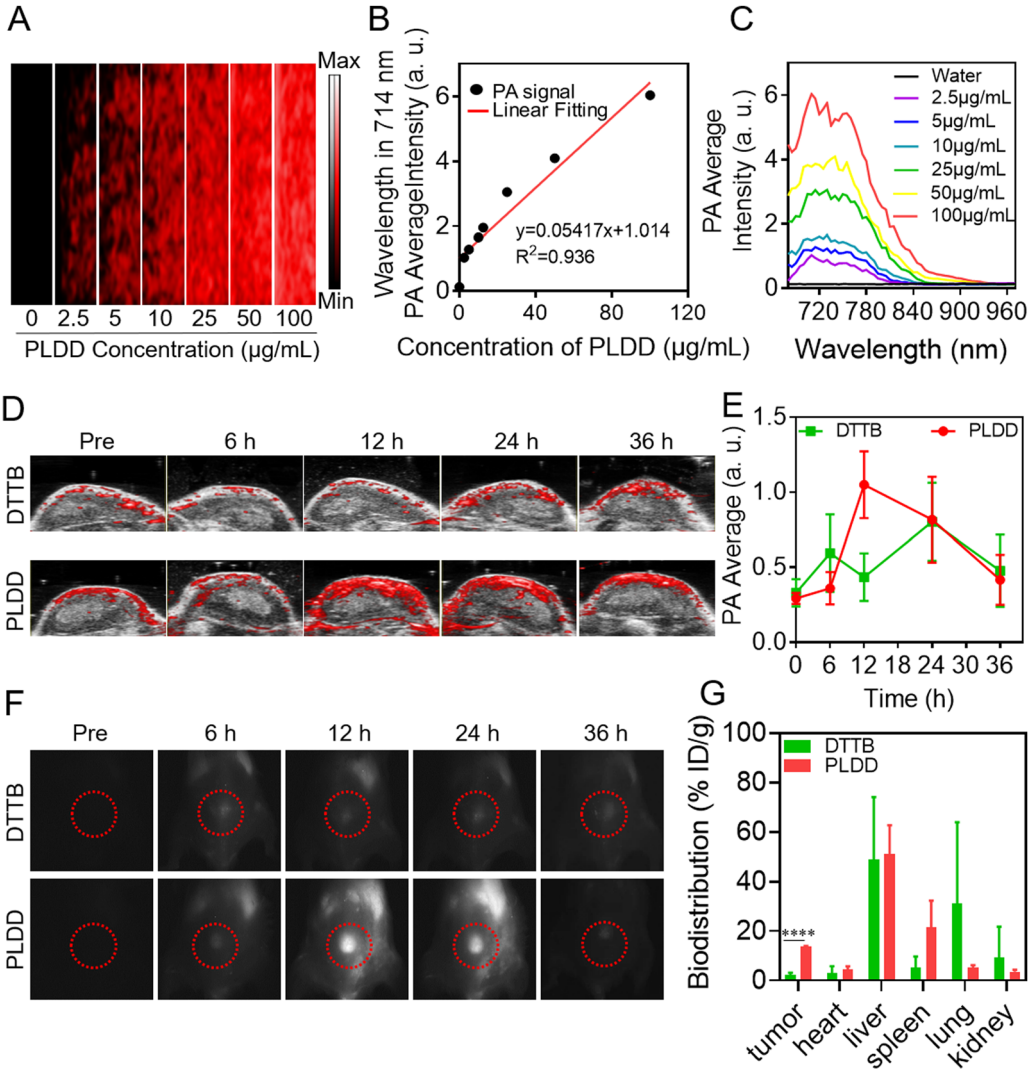

Fig. 3 Dual modal imaging and biodistribution of PLDD *in vivo*. (A) PA imaging of PLDD in 1 × PBS with different concentrations. (B) Linear curve of the concentrations of PLDD *versus* the PA signals at 714 nm. (C) PA spectrum of PLDD at different concentrations scanned with full wavelength. *In vivo* PA imaging (D) and statistical results (E) of LLC tumor-bearing mice at various time intervals after DTTB and PLDD treatments. (F) NIR-II fluorescence imaging of LLC tumor-bearing mice at different time intervals after DTTB and PLDD treatments. (G) Biodistribution of PLDD and DTTB after 12 h of intravenous injection. n = 3.

the STING pathway can be evaluated by detecting DNA damage, STING pathway-related protein expression and interferon-β (INF-β) content. Immunofluorescence was used to detect the formation of phosphorylated H_2AX histone (γ-H_2AX), a key biomarker of DNA double-strand breaks.[48] The PLDD + L group displayed the most abundant γ-H_2AX (red fluorescence) expression in the tumor section (Fig. 4(A)), indicating severe DNA damage. It is noteworthy that the PLDT + L group also showed partial red fluorescence, suggesting that the heat of PTT may cause DNA damage. The above results provide a prerequisite for the activation of the cGAS-STING immune pathway. Western blot was used to detect the expression of STING, IRF3 and ρ-IRF3. As shown in Fig. 4(D), the PLDD + L group increased the expression of the STING protein and promoted the expression of the IRF3 protein and its phosphorylated protein. Moreover, serum levels of INF-β were measured after treatments using an ELISA kit, and the results showed that the INF-β level was obviously elevated in the PLDD + L group (Fig. 4(E)). The above results demonstrate that the triggered release of DMXAA successfully activated the cGAS-STING immune pathway under irradiation, leading to an increase in type I interferon and ultimately enhancing adaptive immunity.

We also examined the expression of relevant immune cells after different treatments. As shown in Fig. 4(F), (G) and Fig. S7A (ESI†), compared with the PBS group, the PLDT + L group achieved only a 2.3-and 3.0-fold increase in $CD11c^+CD86^+$ and $CD11c^+CD80^+$, respectively, while the group of PLDD + L increased the level of $CD11c^+CD86^+$ and $CD11c^+CD80^+$ by 4.5-fold and 3.6-fold, respectively. As shown in Fig. 4(H), (I) and Fig. S7B (ESI†), the PLDT + L group increased only the number of $CD3^+CD4^+$ and $CD3^+CD8^+$ by 13.8% and 6.93% of total leukocytes, respectively, while PLDD + L enhanced the

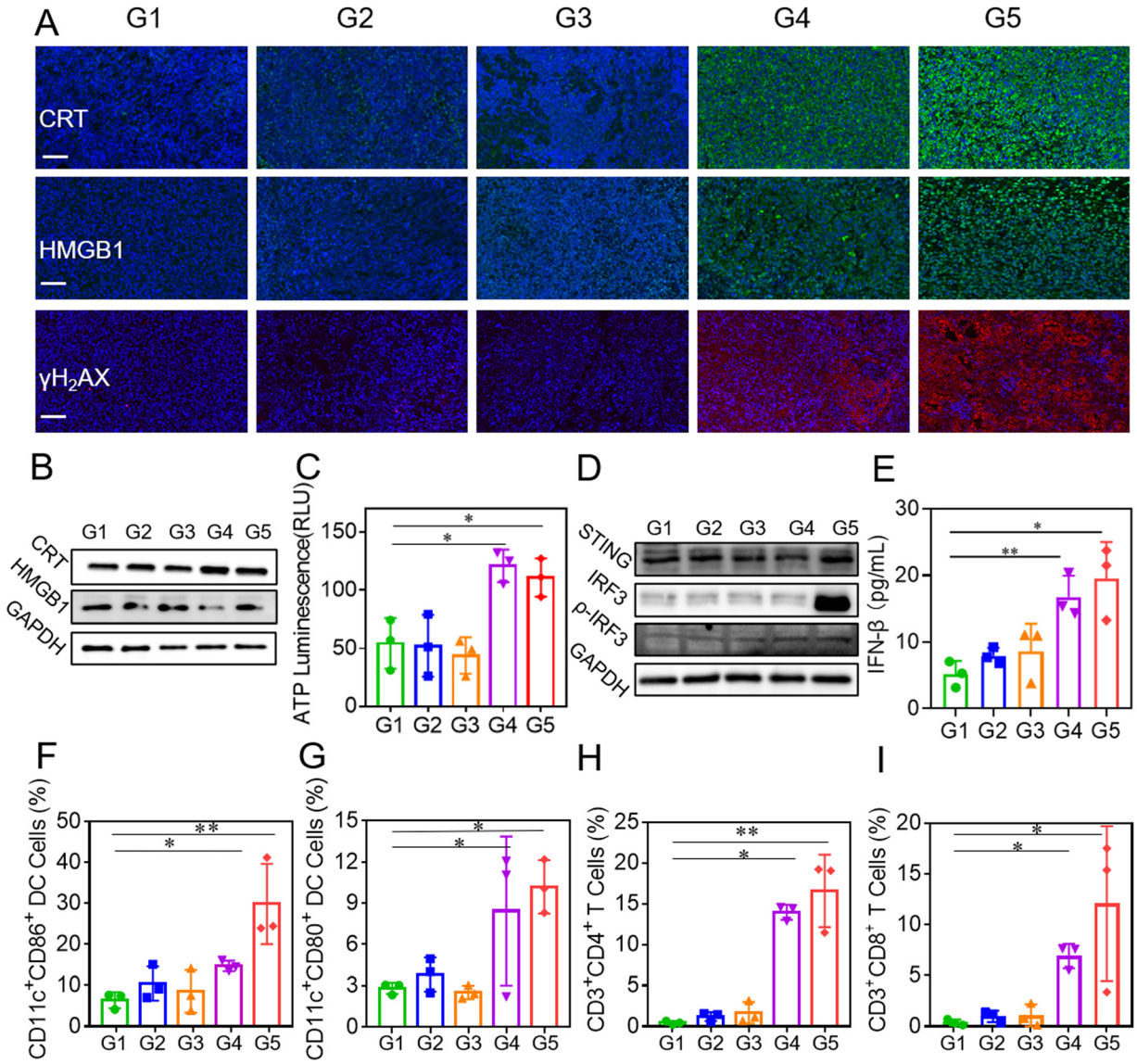

Fig. 4 Boosted adaptive immune response of PLDD. (A) Immunofluorescence of CRT, HMGB1, and γH_2AX in tumor tissues after different treatments. G1, G2, G3, G4, and G5 were PBS, PLDD, Laser, PLDT + L, and PLDD + L, respectively. The scale bar is 100 μm. (B) Western blot analysis of CRT and HMGB1 expression in LLC cells. (C) ATP levels in the supernatants of LLC cells. (D) Western blot analysis of STING, IRF3 and ρ-IRF3 expression on LLC cells. (E) Interferon β (IFN-β) content in serum after different treatments. Flow cytometry analysis of (F) $CD11c^+CD86^+$, (G) $CD11c^+CD80^+$, (H) $CD3^+CD4^+$ and (I) $CD3^+CD8^+$ in LLC tumor tissues after different treatments. $n = 3$. (*$p < 0.05$, **$p < 0.01$).

number of $CD3^+CD4^+$ and $CD3^+CD8^+$ by 16.8% and 12% of total leukocytes, respectively. The above results suggest that the release of DMXAA under irradiation can amplify the adaptive immune response and produce and mature more immune cells, such as DC and T cells, to reverse the tumor immunosuppressive microenvironment and ultimately promote photothermal immunotherapy.

3.5 *In vivo* anti-tumor study of PLDD

The anti-tumor study of PLDD was conducted using LLC tumor-bearing mice. When the tumor grew to approximately 70 mm^3, 100 μL of PLDD, PLDT (500 μg mL^{-1}) or 1 × PBS were intravenously injected into LLC tumor-bearing mice. Then, the mice were locally irradiated by an 808 nm laser after 12 h of administration. The therapeutic effects were assessed daily until the end of the 14 day observation period (Fig. 5(A)). The temperature changes in mice tumors under irradiation were recorded using an infrared thermal image camera, and the PLDT + L and PLDD + L groups showed dramatic temperature increases owing to the excellent photothermal effect of DTTB, which ensured the complete release of the STING agonist (Fig. 5(C) and (D)). The tumor volume and body weight of the mice were recorded daily during the 14 day treatment. As shown in Fig. 5(B), the PLDD + L group achieved the smallest tumor volume among all treatments, indicating the good anti-tumor effect of photothermal immunotherapy. There was no significant change in body weight in each group of mice during the entire treatment procedure, demonstrating that no severe

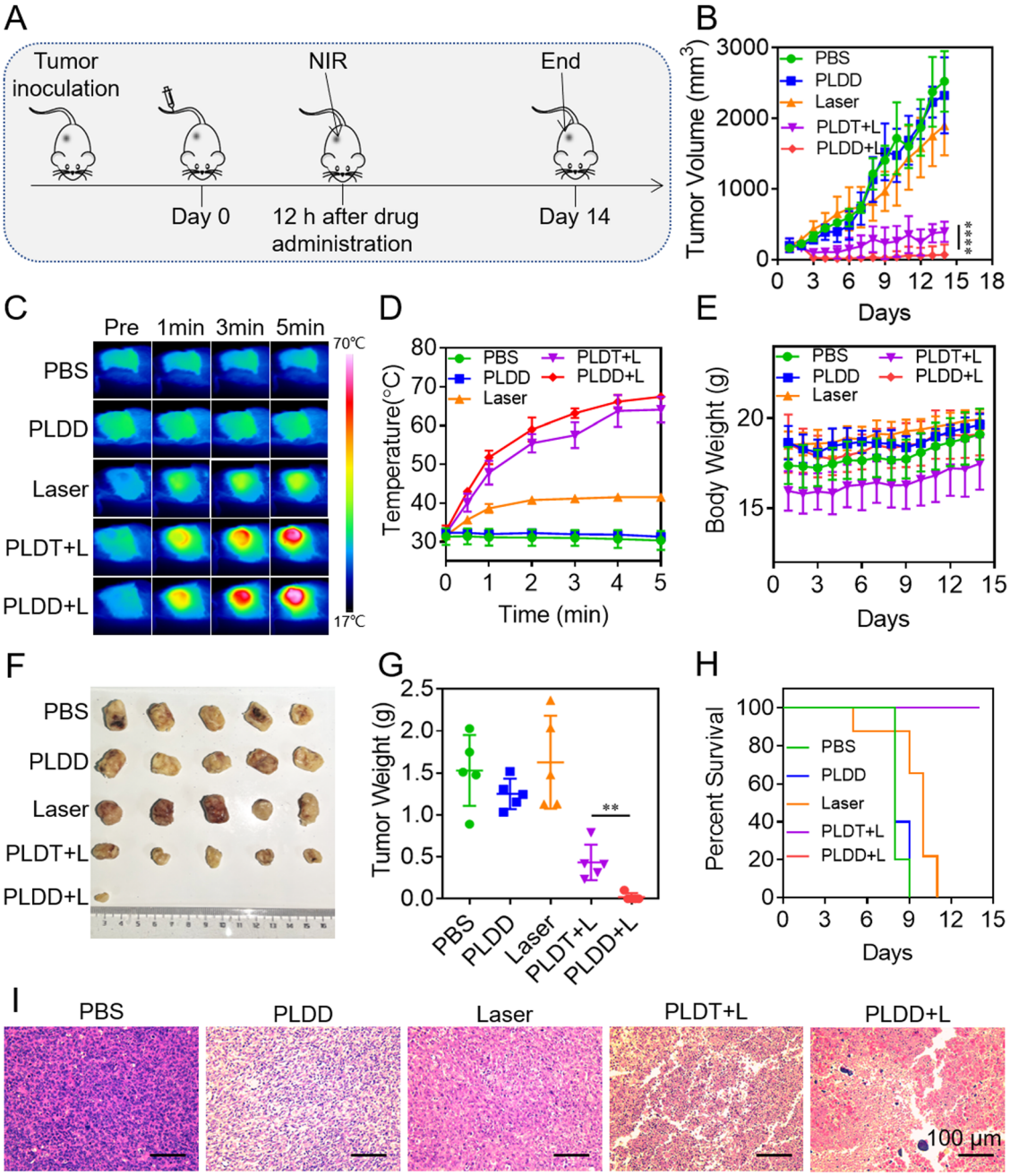

Fig. 5 *In vivo* antitumor activity of PLDD. (A) Schematic diagram of photothermal immunotherapy for LLC tumor-bearing mice. (B) Tumor volume curves of LLC tumor-bearing mice in different treatment groups for 14 days. (C) Photothermal images and (D) temperature curves of the tumor under irradiation. (E) Body weight, (F) tumor photograph, (G) tumor weight, and (H) survival curves of LLC tumor-bearing mice in different treatment groups for 14 days. n = 3. (I) H&E-stained images of tumor tissue on day 14 of treatment. The scale bar is 100 μm. L denotes *laser*. (**$p < 0.01$, ****$p < 0.0001$)

side effects occurred (Fig. 5(E)). After this anti-tumor treatment, the tumors of all groups were dissected to be weighed and photographed, and 80% of the tumors in the PLDD + L group were eliminated (Fig. 5(F) and (G)). Moreover, compared with the groups of PBS, PLDT, and Laser within 12 days of biological death, all mice survived in the PLDT + L and PLDD + L groups after treatment (Fig. 5(H)). We also performed an H&E staining assay of the treated tumor sections (Fig. 5(I)), and the results showed that the tumor treated with PLDD + L had the most severe damage, while the tumor treated with the other treatments was partially damaged or had no obvious damage, indicating the boosted photothermal immunotherapy of PLDD + L by the activation of the STING pathway.

Furthermore, we examined the serum levels of tumor-related factors interleukin-6 (IL-6) and tumor necrosis factor-α (TNF-α) in each group after treatments. IL-6 is an important proinflammatory

cytokine that promotes both innate and adaptive immune responses, whereas TNF-α shows the extent of tumor necrosis. Therefore, assessing the overall levels of IL-6 and TNF-α *in vivo* can reflect the anti-tumor effect of photothermal immunotherapy. As shown in Fig. S8A and B (ESI†), compared with the PBS group, the levels of IL-6 and TNF-α in the serum of mice treated with PLDD + L increased 2.47-fold and 2.3-fold, respectively, than those of the PBS group, and 1.3-fold and 1.1-fold, respectively, than those of the PLDT + L group. These results indicate that the activation of the cGAS-STING pathway can promote the level of immune-related factors and enhance the immune response.

3.6 Biosafety evaluation of PLDD

To evaluate the biosafety of PLDD *in vivo*, we performed H&E staining of the following major organs after the end of treatment (Fig. 6(A)): the heart, liver, spleen, lung, and kidney. The results showed that there were no obvious toxicity or morphological abnormalities in the main organs of each treatment group, indicating that PLDD did not cause any systematic organ damage during the entire photothermal immunotherapy. Then, the whole blood of the mice was collected at the end of the treatment for routine blood tests. As shown in Fig. 6(B), the hematological parameters remained within the normal range

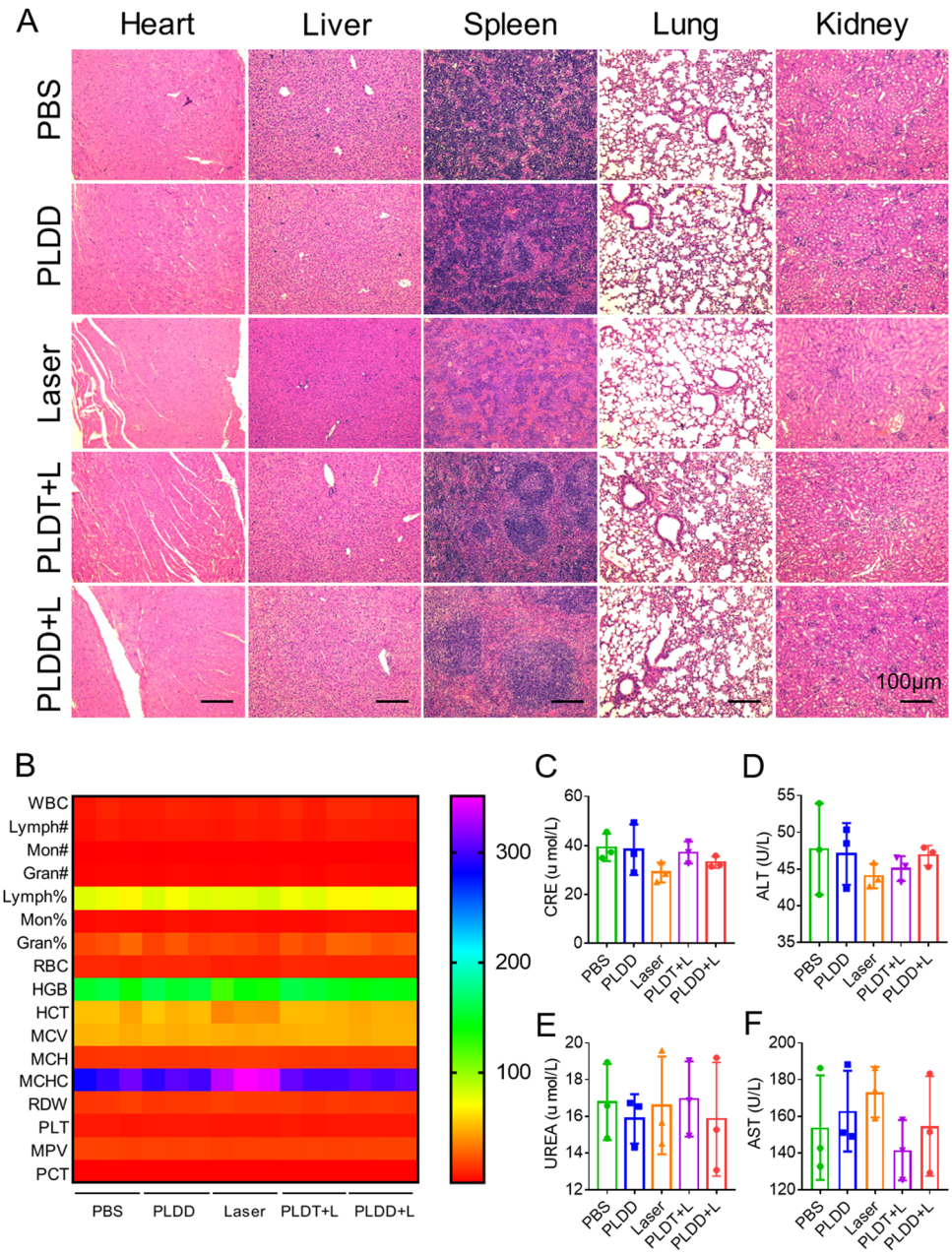

Fig. 6 Biosafety evaluation of PLDD. (A) H&E-stained images of the heart, liver, spleen, lung, and kidney of LLC tumor-bearing mice after 14 days of treatment. The scale bar is 100 μm. (B) Heat map of blood routine in whole blood samples from LLC tumor-bearing mice after 14 days of treatment. Blood biochemical statistics of (C) CRE, (D) ALT, (E) UREA, and (F) AST in LLC tumor-bearing mice after 14 days of treatment. n = 3.

after various treatments. Moreover, we collected serum from mice for biochemical analysis. As shown in Fig. 6(C–F), alanine aminotransferase (ALT), aspartate aminotransferase (AST), urea and uric acid showed no significant hepatorenal toxicity. The above results show that PLDD does not cause any systematic toxicity or liver/kidney injury, indicating its good biocompatibility and biosafety for the photothermal immunotherapy of cancer.

4. Conclusions

In conclusion, a versatile theranostic TSL (PLDD) has been developed for boosting cancer photothermal immunotherapy guided by NIR-II fluorescence and PA dual-modal imaging. The PLDD was constructed using the photothermal agent (DTTB), a STING agonist (DMXAA), phase change materials (LA and SA) and other liposome structure materials. The DTTB endows PLDD with efficient heat production and high resolution of NIR-II fluorescence and PA dual-modal imaging upon irradiation. The DMXAA activated the STING pathway to reverse the immunosuppressive environment of the tumor and promoted the ICD-induced adaptive anti-tumor immunity mainly by increasing the DC maturation and T cell recruitment. Both *in vitro* and *in vivo* experiments demonstrated an excellent photothermal effect, spatiotemporal dual-modal imaging, and boosted adaptive anti-tumor immunity for photothermal immunotherapy. This versatile theranostic TSL with a light-triggered elevation of anti-tumor immunity and spatiotemporal imaging profiles will provide a promising approach for future cancer treatment.

Conflicts of interest

The authors report no conflicts of interest in this work.

Acknowledgements

This work was financially supported by the National Natural Science Foundation of China (grant no. 31971302, 31771099, 81871504, and 82172103) and Natural Science Foundation of Guangdong Province of China (2019A1515011597). The authors also appreciate the support by National Natural Science Foundation of China (grant no. 52173135), Jiangsu Specially Appointed Professorship, Leading Talents of Innovation and Entrepreneurship of Gusu (grant no. ZXL2022496), and the Suzhou Science and Technology Program (grant no. SKY2022039).

References

1 X. Zhu, W. Feng, J. Chang, Y.-W. Tan, J. Li, M. Chen, Y. Sun and F. Li, *Nat. Commun.*, 2016, **7**, 10437.
2 M. Abbas, Q. Zou, S. Li and X. Yan, *Adv. Mater.*, 2017, **29**, 1605021.
3 X. Cheng, R. Sun, L. Yin, Z. Chai, H. Shi and M. Gao, *Adv. Mater.*, 2017, **29**, 1604894.
4 Y. Li, Y. Zhang, Y. Dong, O. U. Akakuru, X. Yao, J. Yi, X. Li, L. Wang, X. Lou, B. Zhu, K. Fan and Z. Qin, *Adv. Mater.*, 2023, **35**, 2210464.
5 Y. Jiang, J. Huang, C. Xu and K. Pu, *Nat. Commun.*, 2021, **12**, 742.
6 Y. Ma, Y. Zhang, X. Li, Y. Zhao, M. Li, W. Jiang, X. Tang, J. Dou, L. Lu, F. Wang and Y. Wang, *ACS Nano*, 2019, **13**, 11967–11980.
7 Q. Chen, L. Xu, C. Liang, C. Wang, R. Peng and Z. Liu, *Nat. Commun.*, 2016, **7**, 13193.
8 G. Qing, X. Zhao, N. Gong, J. Chen, X. Li, Y. Gan, Y. Wang, Z. Zhang, Y. Zhang, W. Guo, Y. Luo and X. J. Liang, *Nat. Commun.*, 2019, **10**, 4336.
9 J. Li, Y. Luo and K. Pu, *Angew. Chem., Int. Ed.*, 2021, **60**, 12682–12705.
10 Y. Ding, Y. Wang and Q. Hu, *Exploration*, 2022, **2**, 20210106.
11 Y. Zheng, Y. Han, Q. Sun and Z. Li, *Exploration*, 2022, **2**, 20210166.
12 I. Noh, Y. Son, W. Jung, M. Kim, D. Kim, H. Shin, Y. C. Kim and S. Jon, *Biomaterials*, 2021, **275**, 120926.
13 W. Li, J. Yang, L. Luo, M. Jiang, B. Qin, H. Yin, C. Zhu, X. Yuan, J. Zhang, Z. Luo, Y. Du, Q. Li, Y. Lou, Y. Qiu and J. You, *Nat. Commun.*, 2019, **10**, 3349.
14 L. Motedayen Aval, J. E. Pease, R. Sharma and D. J. Pinato, *J. Clin. Med.*, 2020, **9**, 3323.
15 X. Zhang, B. Liu, L. Tang, Q. Su, N. Hwang, M. Sehgal, J. Cheng, J. Ma, X. Zhang, Y. Tan, Y. Zhou, Z. Duan, V. R. DeFilippis, U. Viswanathan, J. Kulp, Y. Du, J. T. Guo and J. Chang, *ACS Infect. Dis.*, 2019, **5**, 1139–1149.
16 J. Yan, G. Wang, L. Xie, H. Tian, J. Li, B. Li, W. Sang, W. Li, Z. Zhang and Y. Dai, *Adv. Mater.*, 2022, **34**, e2105783.
17 E. N. Chin, C. Yu, V. F. Vartabedian, Y. Jia, M. Kumar, A. M. Gamo, W. Vernier, S. H. Ali, M. Kissai, D. C. Lazar, N. Nguyen, L. E. Pereira, B. Benish, A. K. Woods, S. B. Joseph, A. Chu, K. A. Johnson, P. N. Sander, F. Martínez-Peña, E. N. Hampton, T. S. Young, D. W. Wolan, A. K. Chatterjee, P. G. Schultz, H. M. Petrassi, J. R. Teijaro and L. L. Lairson, *Science*, 2020, **369**, 993–999.
18 G. Berger, E. H. Knelson, J. L. Jimenez-Macias, M. O. Nowicki, S. Han, E. Panagioti, P. H. Lizotte, K. Adu-Berchie, A. Stafford, N. Dimitrakakis, L. Zhou, E. A. Chiocca, D. J. Mooney, D. A. Barbie and S. E. Lawler, *Proc. Natl. Acad. Sci. U. S. A.*, 2022, **119**, e2111003119.
19 L. Corrales, L. H. Glickman, S. M. McWhirter, D. B. Kanne, K. E. Sivick, G. E. Katibah, S. R. Woo, E. Lemmens, T. Banda, J. J. Leong, K. Metchette, T. W. Dubensky, Jr. and T. F. Gajewski, *Cell Rep.*, 2015, **11**, 1018–1030.
20 C. Falcomatà, S. Bärthel, G. Schneider, R. Rad, M. Schmidt-Supprian and D. Saur, *Cancer Discovery*, 2023, **13**, 278–297.
21 Y. T. Wang, J. Chen, C. W. Chang, J. Jen, T. Y. Huang, C. M. Chen, R. Shen, S. Y. Liang, I. C. Cheng, S. C. Yang, W. W. Lai, K. H. Cheng, T. S. Hsieh, M. Z. Lai, H. C. Cheng, Y. C. Wang and R. H. Chen, *J. Clin. Invest.*, 2017, **127**, 2982–2997.
22 J. Zhao, S. Ma, Y. Xu, X. Si, H. Yao, Z. Huang, Y. Zhang, H. Yu, Z. Tang, W. Song and X. Chen, *Biomaterials*, 2021, **268**, 120542.

23 S. Sun, M. Yu, L. Yu, W. Huang, M. Zhu, Y. Fu, L. Yan, Q. Wang, X. Ji, J. Zhao and M. Wu, *Biomaterials*, 2023, **296**, 122068.
24 M. Hao, L. Zhu, S. Hou, S. Chen, X. Li, K. Li, N. Zhu, S. Chen, L. Xue, C. Ju and C. Zhang, *ACS Nano*, 2023, **17**, 1663–1680.
25 W. Su, M. Tan, Z. Wang, J. Zhang, W. Huang, H. Song, X. Wang, H. Ran, Y. Gao, G. Nie and H. Wang, *Angew. Chem., Int. Ed.*, 2023, **62**, e202218128.
26 X. Gao, G. Lei, B. Wang, Z. Deng, J. Karges, H. Xiao and D. Tan, *Adv. Sci.*, 2023, **10**, e2205241.
27 H. Liang, L. Deng, Y. Hou, X. Meng, X. Huang, E. Rao, W. Zheng, H. Mauceri, M. Mack, M. Xu, Y. X. Fu and R. R. Weichselbaum, *Nat. Commun.*, 2017, **8**, 1736.
28 M. Abri Aghdam, R. Bagheri, J. Mosafer, B. Baradaran, M. Hashemzaei, A. Baghbanzadeh, M. De La Guardia and A. Mokhtarzadeh, *J. Controlled Release*, 2019, **315**, 1–22.
29 M. Ashrafizadeh, M. Delfi, A. Zarrabi, A. Bigham, E. Sharifi, N. Rabiee, A. C. Paiva-Santos, A. P. Kumar, S. C. Tan, K. Hushmandi, J. Ren, E. N. Zare and P. Makvandi, *J. Controlled Release*, 2022, **351**, 50–80.
30 Y. He, L. Lei, J. Cao, X. Yang, S. Cai, F. Tong, D. Huang, H. Mei, K. Luo, H. Gao, B. He and N. A. Peppas, *Sci. Adv.*, 2021, **7**, eaba0776.
31 J. Wu, G. R. Williams, Y. Zhu, T. Hu, H. Wang, W. Zhao, R. Liang, X. Weng and M. Wei, *Biomaterials*, 2021, **273**, 120807.
32 Y. Dai, H. Zhao, K. He, W. Du, Y. Kong, Z. Wang, M. Li, Q. Shen, P. Sun and Q. Fan, *Small*, 2021, **17**, e2102527.
33 C. Ou, W. Na, W. Ge, H. Huang, F. Gao, L. Zhong, Y. Zhao and X. Dong, *Angew. Chem., Int. Ed.*, 2021, **60**, 8157–8163.
34 X. Dai, X. Zhao, Y. Liu, B. Chen, X. Ding, N. Zhao and F. J. Xu, *Small*, 2021, **17**, e2006004.
35 X. Zhen, K. Pu and X. Jiang, *Small*, 2021, **17**, e2004723.
36 Y. Dai, Z. Sun, H. Zhao, D. Qi, X. Li, D. Gao, M. Li, Q. Fan, Q. Shen and W. Huang, *Biomaterials*, 2021, **275**, 120935.
37 D. Liu, L. Liu, F. Liu, M. Zhang, P. Wei and T. Yi, *Adv. Sci.*, 2021, **8**, e2100074.
38 W. Zhang, X. F. Du, B. Liu, C. Li, J. Long, M. X. Zhao, Z. Yao, X. J. Liang and Y. Lai, *ACS Nano*, 2022, **16**, 1421–1435.
39 J. Li, X. Yu, Y. Jiang, S. He, Y. Zhang, Y. Luo and K. Pu, *Adv. Mater.*, 2021, **33**, e2003458.
40 S. Li, H. Chen, H. Liu, L. Liu, Y. Yuan, C. Mao, W. Zhang, X. Zhang, W. Guo, C. S. Lee and X. J. Liang, *ACS Nano*, 2020, **14**, 13681–13690.
41 J. E. Talmadge and D. I. Gabrilovich, *Nat. Rev. Cancer*, 2013, **13**, 739–752.
42 Z. Tao, B. B. Toms, J. Goodisman and T. Asefa, *Chem. Res. Toxicol.*, 2009, **22**, 1869–1880.
43 A. L. Klibanov, K. Maruyama, V. P. Torchilin and L. Huang, *FEBS Lett.*, 1990, **268**, 235–237.
44 Z. Huang, D. Yao, Q. Ye, H. Jiang, R. Gu, C. Ji, J. Wu, Y. Hu and A. Yuan, *ACS Nano*, 2021, **15**, 8450–8465.
45 Q. Zhu, F. Sun, T. Li, M. Zhou, J. Ye, A. Ji, H. Wang, C. Ding, H. Chen, Z. Xu and H. Yu, *Small*, 2021, **17**, e2007882.
46 C. Wang, Z. Sun, C. Zhao, Z. Zhang, H. Wang, Y. Liu, Y. Guo, B. Zhang, L. Gu, Y. Yu, Y. Hu and J. Wu, *J. Controlled Release*, 2021, **331**, 480–490.
47 C. Zhang, S. He, Z. Zeng, P. Cheng and K. Pu, *Angew. Chem., Int. Ed.*, 2022, **61**, e202114957.
48 L. Corrales, S. R. Woo, J. B. Williams, S. M. McWhirter, T. W. Dubensky, Jr. and T. F. Gajewski, *J. Immunol.*, 2016, **196**, 3191–3198.

